



Debye-scale Solitary Structures in the Martian Magnetosheath

Bharati Kakad¹, Amar Kakad¹, Harikrishnan Aravindakshan¹, and Ioannis Kourakis^{2,3}¹Indian Institute of Geomagnetism, New Panvel, Navi Mumbai 410218, India; bkakad9@gmail.com²Department of Mathematics, College of Arts and Sciences, Khalifa University, Abu Dhabi, UAE³Space and Planetary Science Center, Khalifa University, Abu Dhabi, UAE

Received 2022 April 17; revised 2022 June 1; accepted 2022 June 10; published 2022 August 1

Abstract

We present an analysis of 450 solitary wave pulses observed by the Langmuir Probe and Waves instrument on the Mars Atmosphere and Volatile Evolution spacecraft during its five passes around Mars on 2015 February 9. The magnitude and duration of these pulses vary between 1 and 25 mV m⁻¹ and 0.2–1.7 ms, respectively. The ambient plasma conditions suggest that these pulses are quasi-parallel to the ambient magnetic field and can be considered electrostatic. These pulses are dominantly seen in the dawn (5–6 LT) and afternoon-dusk (15–18 LT) sectors at an altitude of 1000–3500 km. The frequencies of these electric field pulses are close to the ion plasma frequency (i.e., $f_{pi} \leq f_{ef} \ll f_{pe}$), which suggests that their formation is governed by ion dynamics. The computer simulation performed for the Martian magnetosheath plasma hints that these pulses are ion-acoustic solitary waves generated by drifted ion and electron populations and their spatial scales are in the range of few ion Debye lengths (1.65–10 λ_{di}). This is the first study to report and model solitary wave structures in the Martian magnetosheath.

Unified Astronomy Thesaurus concepts: [Space plasmas \(1544\)](#); [Planetary magnetospheres \(997\)](#); [Mars \(1007\)](#)

1. Introduction

Earth and planetary space plasma environments support a variety of electromagnetic and electrostatic waves. These plasma waves are widely studied using observations, theory, and simulations to enhance our knowledge of the ambient plasma conditions and fundamental physical processes operational in those regions. These plasma waves play an important role in the transport and acceleration/deceleration of charged particle processes. In various regions of the Earth's magnetosphere, broadband electrostatic noise (BEN) is observed (Matsumoto et al. 1994; Bale et al. 1998; Ergun et al. 1998). BEN consist of a series of electrostatic solitary waves (ESWs) and their characteristics are determined by the ambient plasma population therein. These electric field structures are generally bipolar in nature, and they are identified as ion/electron acoustic waves or as electron/ion phase-space holes (Omura et al. 1996; Lakhina et al. 2011; Kakad et al. 2019; Pickett 2021). Observations of solitary wave structures are not limited to Earth; they are also observed in other planetary magnetospheres (Williams et al. 2006; Malaspina et al. 2020), and astrophysical plasma environments (Tao et al. 2012; Mozer et al. 2021a, 2021b).

Planet Mars does not have an intrinsic magnetic field but the conductive ionosphere and mass loading on the Martian atmosphere act as an obstacle to the solar wind and form the bow shock and induced magnetosphere (Nagy et al. 2004; Vaisberg et al. 2017). The magnetosphere of Mars has been studied by various missions like Phobos, Mars Global Surveyor, Mars Express, Mars Odyssey, and Mars Science Laboratory. Recently, the Mars Atmosphere and Volatile Evolution (MAVEN) mission has provided an excellent opportunity to explore plasma processes in the magnetosphere of Mars (Romanelli et al. 2018; Vaisberg et al. 2018). Different

plasma waves like electron plasma oscillations and electron-induced whistler waves have been observed in the Martian upper atmosphere (Grard et al. 1989; Trotignon et al. 1991; Harada et al. 2016). This suggests that although Mars possesses an induced mini magnetosphere, it is highly dynamic and capable of generating various plasma waves. Thus, the investigation of electric/magnetic field observations in the Martian atmosphere can provide meaningful information about the different plasma wave processes operating in such a dynamic region. The MAVEN spacecraft carries the Langmuir Probe and Waves (LPW) instrument, which records electric field measurements at an altitude of 150–6200 km. This altitudinal range covers the ionosphere-magnetosphere regions of Mars. Recently, ambipolar electric field structures in the ionosphere of Mars have been studied by Akbari et al. (2019). These ambipolar electric fields are associated with pressure gradients, have a magnitude of the order of microvolts per meter, a large spatial extent, and play an important role in the escape of charged particles from Mars' atmosphere. In addition, owing to the dynamical behavior of the magnetosphere, and the observation of magnetic reconnection in the Martian magnetosphere, one anticipates the presence of solitary waves in the Martian upper atmosphere. Localized electric field structures in the magnetosheath regions of Mars have not been reported so far. If the presence of solitary structures is confirmed, then it will provide an explanation for the plasma heating and plasma transport frequently observed in its magnetosphere (Pérez-de Tejada 1987; Lundin et al. 2006). In this paper, we present the characteristics of the bipolar electric field pulses observed in the Martian magnetosheath region. Furthermore, we present theory and numerical simulations to investigate the generation mechanism of these pulses in the magnetosheath region of Mars.

This article is organized as follows. The data used in the study are elaborated in Section 2. The results are presented and discussed in Section 3. The article is summarized and concluded in Section 4.



Original content from this work may be used under the terms of the [Creative Commons Attribution 4.0 licence](#). Any further distribution of this work must maintain attribution to the author(s) and the title of the work, journal citation and DOI.

2. Data Analysis

The MAVEN spacecraft mission is devoted to studying different phenomena in the atmosphere near Mars via various instruments mounted on it. We used data from the LPW, MAVEN Solar Wind Electron Analyzer (SWEA), and Solar Wind Ion Analyzer (SWIA) instruments (Andersson et al. 2015; Halekas et al. 2015; Mitchell et al. 2016). The burst mode medium-frequency (100 Hz–32 kHz), high-amplitude calibrated electric field data from the LPW instrument on 2015 February 9 is utilized in the present study. It measures the electric field in one direction using two approximately 7 m ridged booms such that the sensors are aligned with the y -axis of the spacecraft’s coordinate system. Depending on the telemetry time, a total of 2779 burst mode intervals of 62.5–375 ms with continuous electric field observations were available. We examined these burst mode events to identify the existence of bipolar electric field pulses. To understand the ambient plasma conditions, we used calibrated survey rate omni-directional differential energy spectra data (i.e., svy-spec) in units of differential energy flux ($\text{eV cm}^{-2} \text{ s sr eV}$). The SWIA and SWEA instruments measure differential ion and electron flux of 5 eV–25 keV, and 3–4600 eV, respectively. The high-resolution MAVEN MAG calibrated magnetic field vector data acquired by the fluxgate magnetometer instrument (Connerney et al. 2015) in the payload/spacecraft coordinate system are used. All the abovementioned data sets are available at <https://pds-ppi.igpp.ucla.edu>. In addition, key parameters, derived from different in situ instruments (NGIMS, EUV, LPW, MAG, SEP, STATIC, SWEA, and SWIA) on the MAVEN spacecraft, are available at <https://cdaweb.gsfc.nasa.gov/>. These key parameters are available at 4 or 8 s resolution and are used to obtain the electron/ion density, solar wind velocity, altitude, local time, etc.

3. Results and Discussion

In this section, we elaborate on the details of observed solitary wave pulses and their characteristics. Further, we demonstrate the generation mechanism of these pulses using theory and simulation.

3.1. Examples of Solitary Wave Pulses

On 2015 February 9, the MAVEN spacecraft (orbital time 4.5 hr) made approximately five passes around Mars. During these passes, LPW observed several bipolar electric field pulses in the medium frequency range. We could identify a total of 450 bipolar electric field pulses. One example of such a series of bipolar electric field pulses is shown in Figure 1(a) and its spectrogram is shown in Figure 1(b). Time on the x -axis is in milliseconds starting after 9.9651 UT hr (09:57:54:360 hh:mm:ss:mss). The plotted electric field is the y component of electric field (i.e., E_y) recorded in spacecraft coordinate system. In panel (b), the ion plasma frequency is shown by the black dashed horizontal line. Another example of a series of bipolar pulses is shown in Figure 2. Here, the time on the x -axis is in milliseconds starting after 10.0517 UT hr (10:03:06:120 hh:mm:ss:mss). The important features of the observed events are that the electric field pulses have durations (peak-to-peak time difference) of ≤ 1 ms and their frequencies are close to the ambient ion plasma frequency. We examined the ambient plasma conditions during the occurrence of the electric field pulses, as shown in Figures 1 and 2. Figure 3 shows the

electron (black) and ion (red) densities in panel (a), the angle between magnetic field (\mathbf{B}) and plasma bulk flow velocity (\mathbf{V}_i) in the Mars Solar Orbital (MSO) coordinate system in panel (b), the magnetic field components [B_x , B_y , B_z] and the total magnetic field strength B in spacecraft coordinate system in panel (c), the angle between magnetic field (\mathbf{B}) and E_y in the spacecraft coordinate system in panel (d), and the plasma bulk flow velocity components [V_{ix} , V_{iy} , V_{iz}] along with the total bulk flow speed (V_i) in the MSO coordinate system in panel (e) as a function of time in UT hours. The start time of example 1 and example 2 (shown in Figures 1 and 2) are marked by vertical dashed lines in panel (a). One can see that the electron and ion plasma densities vary in the close range between 10 and 20/cc. From Figure 3(b) we can see that the angle between the solar wind velocity and the ambient magnetic field vector is around 110° , which suggests that the solar wind is quasi-perpendicular to the ambient magnetic field. As can be seen in Figure 3(d), the angle, θ , between E_y and \mathbf{B} is approximately 30° , which indicates that the observed electric field structures are quasi-parallel to the ambient magnetic field. This confirms the electrostatic nature of the observed electric field pulses. Therefore, we can treat them as ESWs. As can be seen in panel (e), the solar wind bulk speed was around 150 km s^{-1} during this time. These electric field pulses are quasi-parallel to the ambient magnetic field. In such a situation, there could be some weak magnetic field fluctuations associated with this wave mode but it cannot be checked as MAVEN magnetic field measurement has a sampling capacity of 32 Hz (Connerney et al. 2015), whereas ion-acoustic electric field pulses have frequency close to a few kilohertz.

3.2. Characteristics of Solitary Pulses

In the previous section, we looked at two examples wherein a series of electric field pulses were observed in Mars’ atmosphere. We identified such distinct electric field pulses and noted their characteristics, like the maximum electric field (E_{\max}), the minimum electric field (E_{\min}), the duration δt (peak-to-peak time difference), and their corresponding local time, altitude, ambient electron (n_e), and ion (n_i) density. The ambient plasma density is used to calculate the ion and electron plasma frequencies (i.e., $\omega_{ps} = \sqrt{n_s e^2 / m_s \epsilon_0}$; here s represents species). In Figure 4(a), the occurrences of bipolar electric field pulses are denoted by red “+” signs on the three-dimensional trajectory of MAVEN (green color) around Mars on 2015 February 9. Overall, we identified 450 bipolar electric field pulses. The minimum $|E_{\min}|$ and maximum E_{\max} electric fields associated with these pulses are shown in Figure 4(b). The minimum and maximum amplitudes of the electric field pulses are in close range, which indicates that these electric field structures are nearly symmetric in nature. The strength of the electric field of these pulses varies between 1 and 25 mV m^{-1} . Next, we examined the altitude and local time of these electric field pulses. The normalized probability distribution function of local time encountered by the MAVEN spacecraft during its trajectory around Mars (black) and the normalized probability distribution function of local time corresponding to the occurrence of electric field pulses (red color) are shown in Figure 4(c). Here, the sum of normalized distribution is 1, and it represents the total number of occurrences available to estimate respective distributions. For example, we had a total of 11,655 local time occurrences of the MAVEN spacecraft during its trajectory around Mars and a total of 450

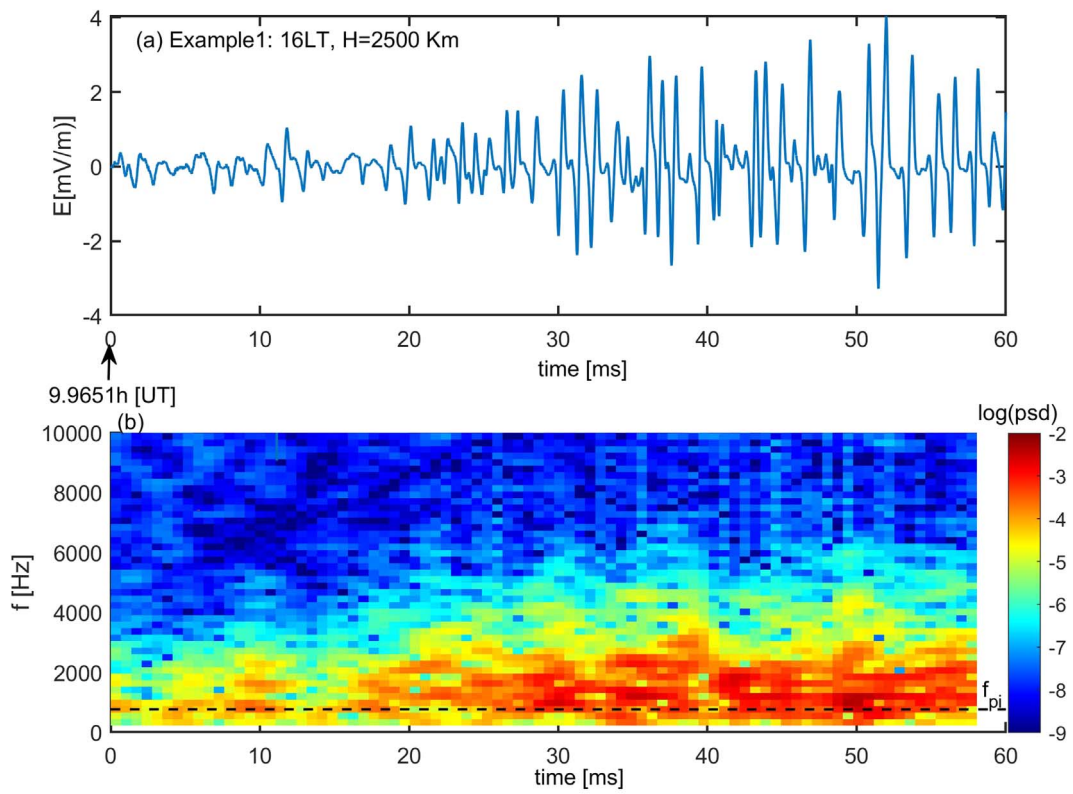


Figure 1. An example of a series of bipolar electric field pulses observed by the LPW instrument on 2015 February 9 is shown in panel (a) and its spectrogram is shown in panel (b). The time-frequency domain resolution of the spectrogram is 0.69 ms–0.2 kHz. Time is in milliseconds after 9.9651 UT hr. The plotted electric field is the y component of electric field (i.e., E_y) recorded in spacecraft coordinate system. The ion plasma frequency, f_{pi} is shown by the black dotted horizontal line in the lower panel. The power spectral density (PSD) is in units of square millivolts per hertz.

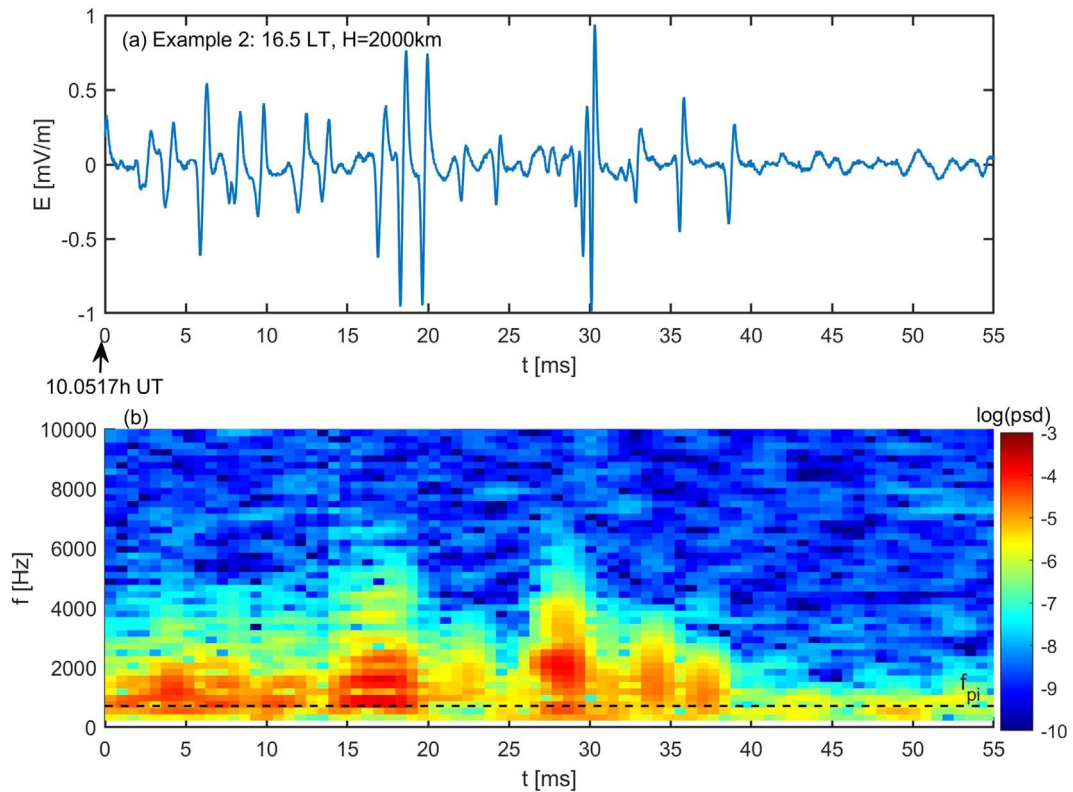


Figure 2. An example of a series of bipolar electric field pulses observed by the LPW instrument on 2015 February 9 is shown in panel (a) and its spectrogram is shown in panel (b). Time is in milliseconds after 10.0517 UT hr. The plotted electric field is the y component of electric field (i.e., E_y) recorded in spacecraft coordinate system. The ion plasma frequency, f_{pi} is shown by the black dotted horizontal line in the lower panel. The PSD is in units of square millivolts per hertz.

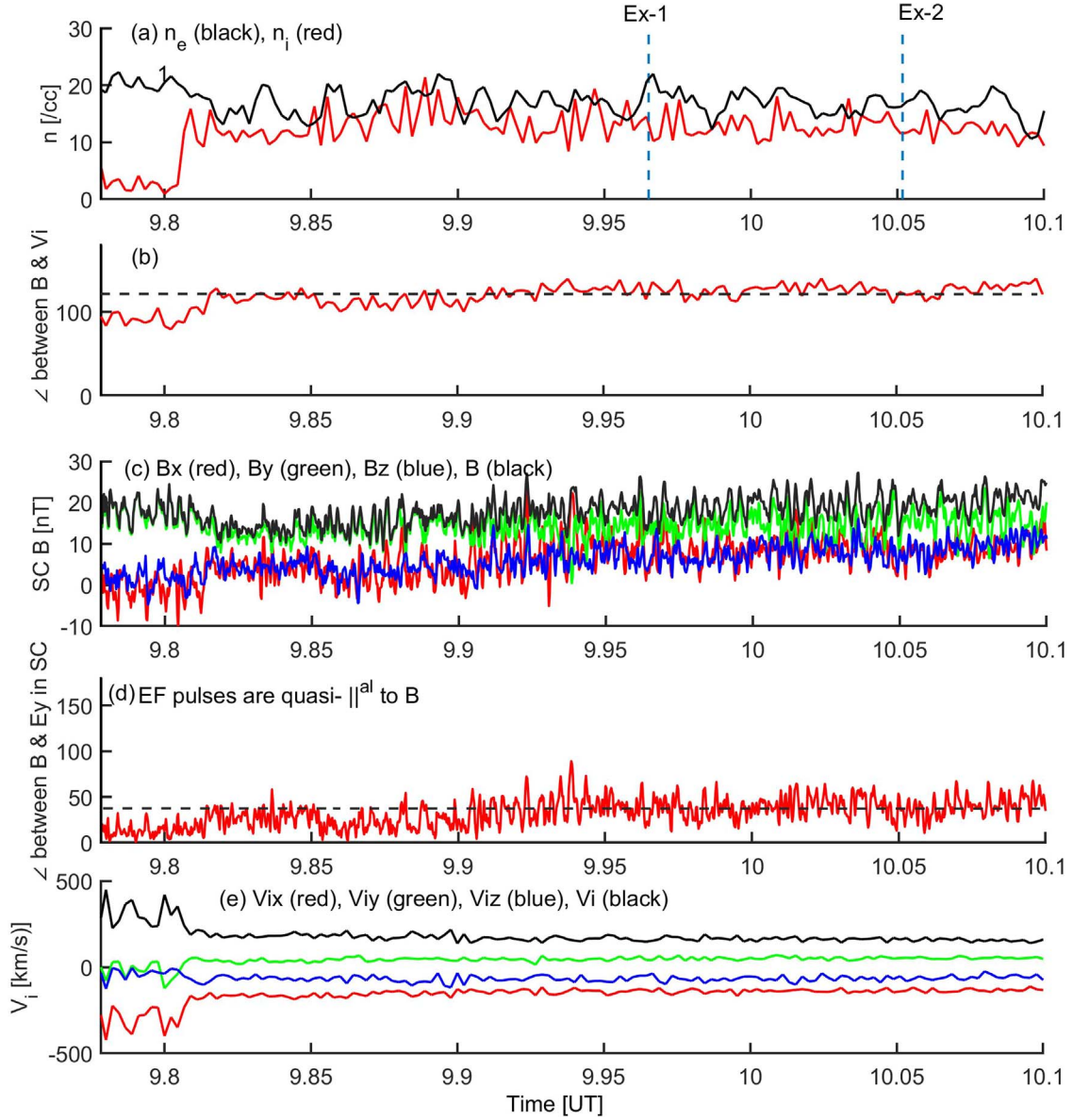


Figure 3. (a) The electron and ion densities, (b) the angle between the magnetic field (\mathbf{B}) and the plasma bulk flow velocity (V_i) in the MSO coordinate system, (c) the magnetic field components [B_x , B_y , B_z] and total magnetic field strength B in the spacecraft’s coordinate system, (d) the angle between magnetic field (\mathbf{B}) and E_y in the spacecraft’s coordinate system, (e) plasma bulk flow velocity components [V_{ix} , V_{iy} , V_{iz}], and the total bulk flow speed (V_i) in the MSO coordinate system are shown as a function of time (in UT hours).

simultaneous occurrences of local time corresponding to the time of the electric field pulses. In a similar way, we obtained the normalized probability distribution function for the altitude encountered by the MAVEN spacecraft during its trajectory around Mars (black) and the normalized probability distribution function of altitudes corresponding to the occurrence of electric field pulses (red color) as plotted in Figure 4(d). Figures 4(c)–(d) reveal that these electric field pulses are predominantly seen in the dawn, 5–6 LT and dusk sector 15–18 LT at an altitude of 1000–3500 km.

In a further investigation, we considered the bipolar electric field pulses that are observed at an altitude of 1000–3500 km (total of 371 events). The distribution of the pulse duration, δt of electric field pulses, and their associated frequencies, $f_{ef} = 1/\delta t$, are plotted in Figures 5(a) and 5(b), respectively. The distribution of the ion plasma frequency ($f_{pi} = \omega_{pi}/2\pi$) and the electron plasma frequency ($f_{pe} = \omega_{pe}/2\pi$) calculated from

the ambient ion and electron densities are plotted in Figures 5(c) and (d), respectively. It may be noted that simultaneous, electron density information was only available for 117 electric field pulses. We found that the duration and frequency of electric field pulses are dominantly seen in the range of 0.2–1 ms i.e., 1–5 kHz, respectively, with an average duration of electric field pulses of 0.60 ms and average frequency of 2.1 kHz. The ambient plasma conditions suggest that the ion plasma frequency varies between 0.2 and 1 kHz with an average close to 0.65 kHz, whereas the electron plasma frequency varies between 20 and 50 kHz with an average close to 35 kHz. It clearly indicates that the electric field pulses observed at an altitude of 1000–3500 km have a frequency close to the ion plasma frequency, which is much less than the electron plasma frequency, i.e., $f_{pi} \leq f_{ef} \ll f_{pe}$. This hints that the generation of these electric field pulses might have been associated with ion dynamics. Also, one can see frequency

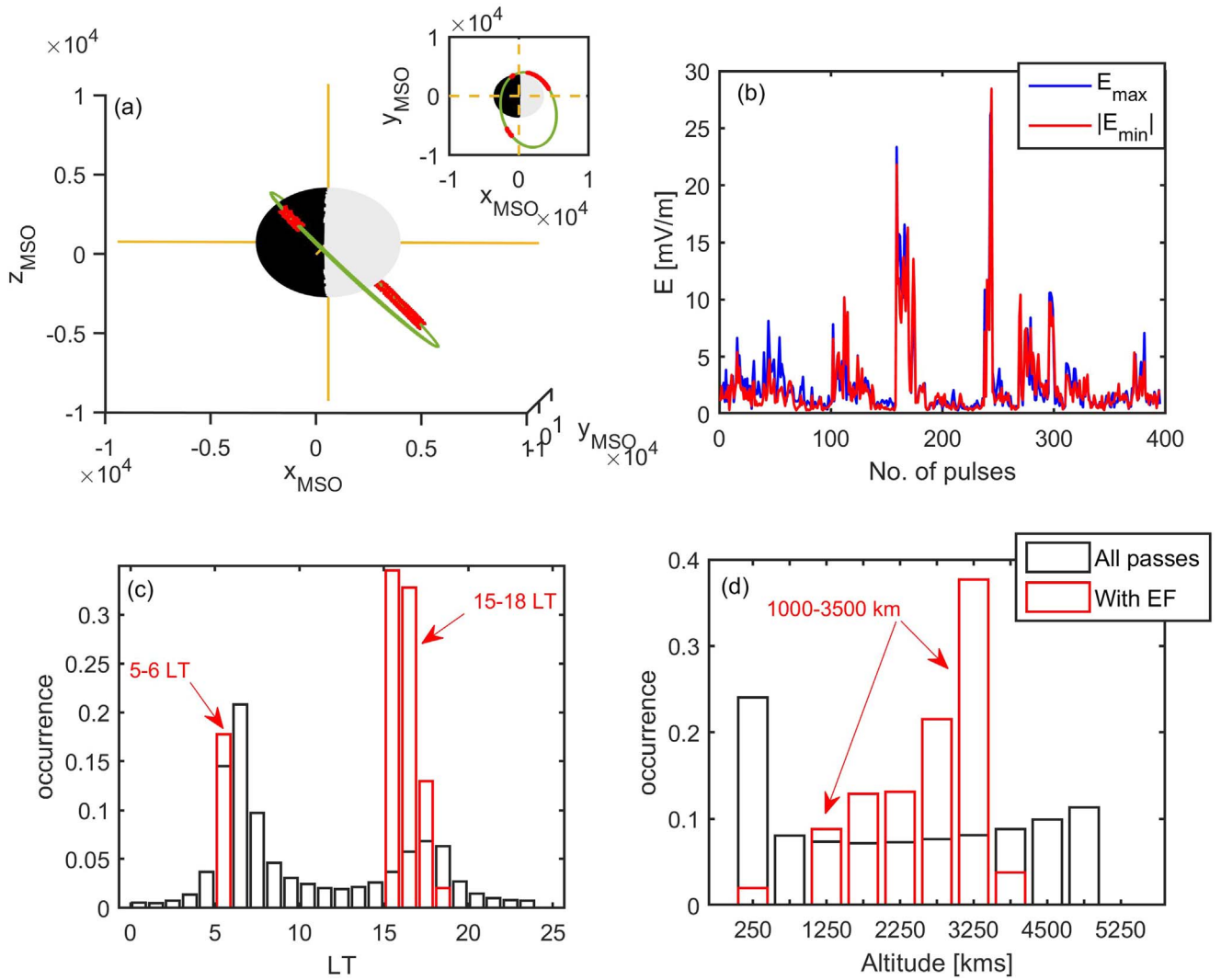


Figure 4. (a) Three-dimensional view of MAVEN trajectory (green color) around Mars on 2015 February 9. The occurrences of bipolar electric field pulses are shown by red “+” signs. (b) The minimum $|E_{\text{min}}|$ and maximum E_{max} electric fields associated with bipolar electric field structures are shown for 450 pulses. (c) The normalized probability distribution function of the local time encountered by MAVEN during its trajectory around Mars (black) and the normalized probability distribution function of the local time corresponding to the occurrence of electric field pulses (red color) are shown. (d) The normalized probability distribution function of the altitude encountered by MAVEN during its trajectory around Mars (black) and the normalized probability distribution function of altitudes corresponding to the occurrence of electric field pulses (red color) are shown.

broadening in the spectrograms shown in Figures 1(b) and 2(b). Here, the peak average PSD is localized close to ion plasma frequency; however, there is a broadening (Δf) in the spectra, which is estimated to be 300–400 Hz. Here, Δf is the width in the frequency domain, where the peak average PSD decreases to 50%. Generally, ion-acoustic waves have frequencies close to or less than f_{pi} . However, as suggested by Akimoto & Winske (1985), when these waves are observed the wave frequency may get Doppler shifted by a few kilohertz due to the motion of the solar wind. This could be a possible reason for getting $f_{\text{pi}} \leq f_{\text{et}} < f_{\text{pe}}$ for observed electric field pulses. These ion-acoustic type solitary waves can have different generation mechanisms, e.g., they can be ion-acoustic solitary waves (Kakad et al. 2013) or ion holes (Akimoto & Winske 1985; Aravindakshan et al. 2020) driven by an ion-beam instability. In order to look into their possible generation mechanisms, we performed a fluid simulation, which is discussed in the next subsections.

3.3. Simulation of Electrostatic Solitary Pulses

In order to examine the ambient plasma conditions, we looked into ion and electron flux observations. The MAVEN spacecraft carry Solar Wind Ion Analyzer (SWIA) and Solar Wind electron Analyzer (SWEA) instruments that record the ion and electron flux. On 2015 February 9, SWIA observed ion energy flux as a function of time and energy as depicted in Figure 6(a). Similarly, SWEA observed electron energy flux as a function of time and energy, as shown in Figure 6(c). As detailed in Table 1, bipolar pulses are observed in 10 different time slots marked by vertical dotted lines in Figure 6(e), which depicts the variation in the altitude of the MAVEN spacecraft as a function of time on 2015 February 9. For the respective time slots, we averaged the ion and electron fluxes to get their energy spectra. These estimated ion and electron flux are plotted as a function of energy in Figures 6 (b) and (d), respectively, with different colored dashed–dotted lines. The

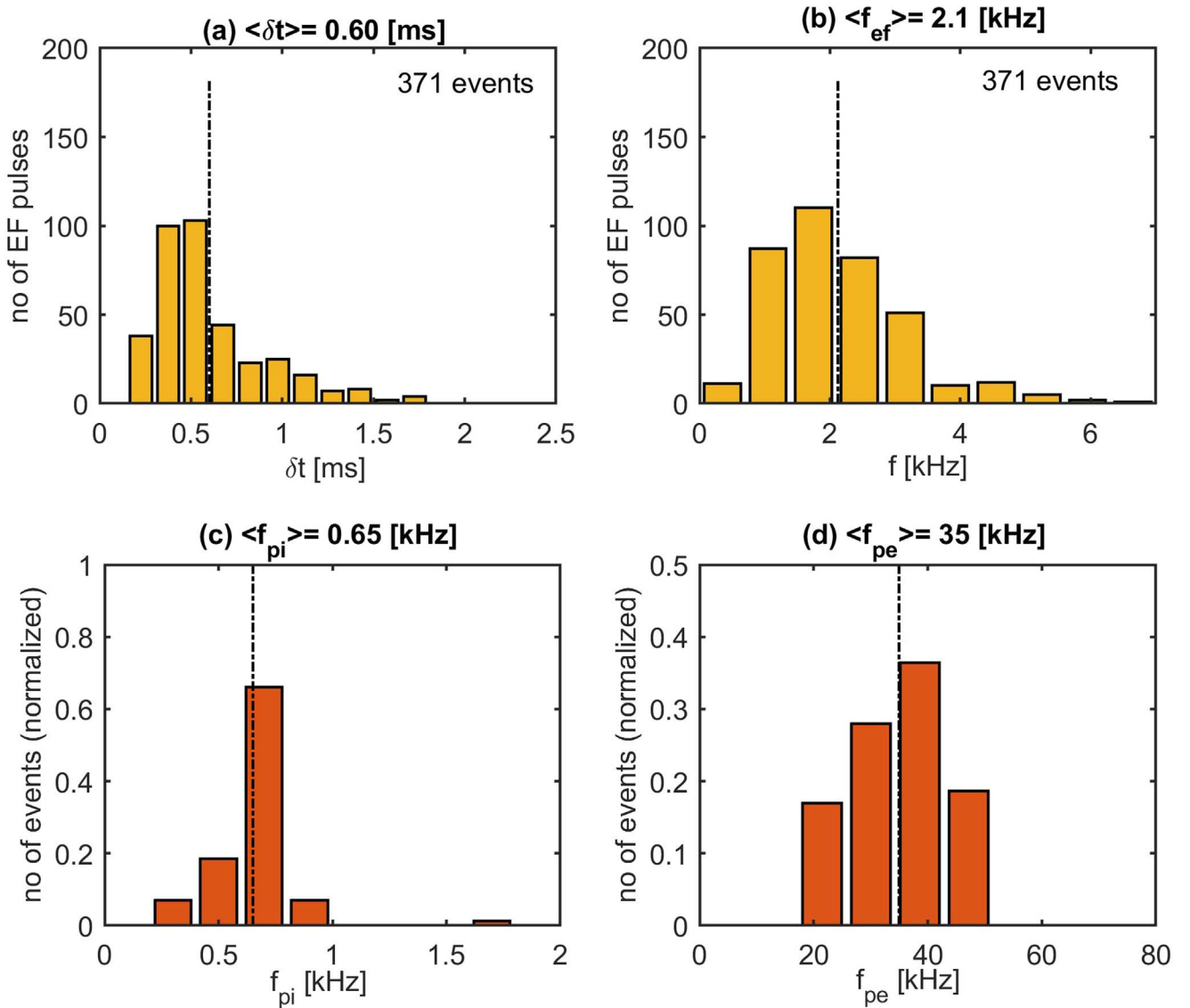


Figure 5. (a) The distribution of duration, δt (peak-to-peak time difference) of electric field pulses. The average duration is 0.60 ms. (b) The distribution of the frequency of these electric field pulses ($f_{ef} = 1/\delta t$). The average frequency of pulses is approximately 2.12 kHz. Based on the measurement of the ambient plasma density, the normalized distribution of the ion plasma frequency (f_{pi}) and electron plasma frequency (f_{pe}) during the occurrence of these electric field pulses are shown in panels (c) and (d), respectively. The sum of the normalized distribution shown in panels (c) and (d) is unity and it corresponds to the total number of density data available to estimate these distributions. In the case of ion and electron plasma frequency, we have a total of 371 and 118 density data points, respectively.

black curves in Figures 6(b) and (d) represent the average flux. It can be seen that the ion flux and electron flux peaks are close to 300 and 60 eV, indicating the difference in the temperatures of the ambient plasma populations. We considered these two plasma populations while modeling these solitary pulses. Mars does not have an intrinsic global magnetic field like Earth does, but it has an induced magnetosphere resulting from the solar wind interactions with the upper atmosphere of Mars (Nagy et al. 2004; Ma et al. 2004). We used the model proposed by Trotignon et al. (2006) to get the location of Mars’ bow shock and magnetopause, which is shown in Figure 7(a) superimposed with a red “+” sign, representing the occurrences of 371 electric field pulses. In addition, the direction of the ambient magnetic field in the dusk sector, during the occurrence of electric field pulses shown in Figures 1 and 2, is depicted by the black arrow. Figure 7(a) reveals that the solitary pulses are observed dominantly in the magnetosheath

region of Mars. A sketch of the ambient plasma and magnetic field conditions along with electric field pulses is illustrated in Figure 7(b). We considered the simulation model based on this schematic. From Figure 3(b), one can see that the solar wind is quasi-perpendicular (at an angle of $\sim 110^\circ$ in the $+B$ direction); therefore, the solar wind ions and electrons have a velocity component antiparallel to the magnetic field such that speed is approximately $V_i \cos(\theta)$, where $\theta = 180^\circ - 110^\circ$. Along similar lines, as shown in Figure 3(d), the angle between \mathbf{B} and E_y is around 30° , which affirms the quasi-parallel propagation of the bipolar pulses illustrated in the schematic shown in Figure 7(b).

We considered a homogeneous, collisionless two species plasma consisting of electrons and ions (H^+ ions) in the simulation model. The ambient plasma parameters for ions and electrons are given in Table 2. The ions and electrons are considered to be fluid and their dynamic is incorporated into the simulation model using the following model equations viz.,

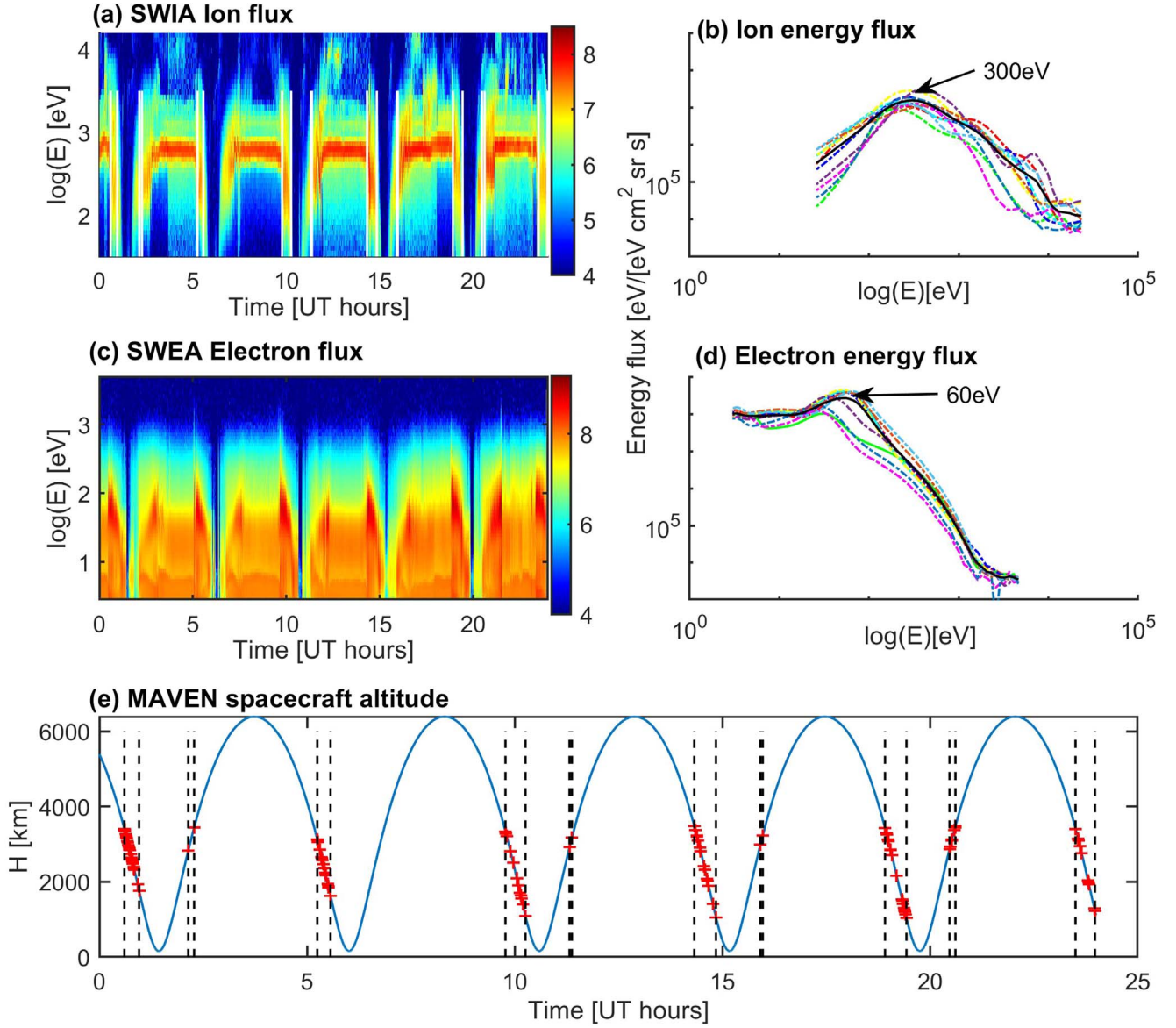


Figure 6. (a) The differential ion energy flux observed by SWIA as a function of time and energy. (b) The differential ion energy flux is averaged for the time slots given in Table 1 and ion energy flux is plotted with dashed–dotted lines. Their average ion energy flux is shown by the black line, which peaks around 300 eV. (c) SWEA observed differential electron energy flux as a function of time and energy. (d) The electron energy flux is averaged for the time slots given in Table 1 and the respective electron flux is plotted as a function of energy with dashed–dotted lines. The average electron energy flux is shown by the black line, which peaks around 60 eV. (e) The altitude of the Mavem spacecraft as a function of time with the occurrence of electric field pulses marked with red “+” signs.

the continuity, momentum, and pressure equations of each species, and the Poisson equation (Kakad et al. 2014) given by

$$\frac{\partial n_j}{\partial t} + \frac{\partial(n_j v_j)}{\partial x} = 0, \quad (1)$$

$$\frac{\partial v_j}{\partial t} + v_j \frac{\partial v_j}{\partial x} + \frac{1}{m_j n_j} \frac{\partial P_j}{\partial x} - \frac{q_j}{m_j} E = 0, \quad (2)$$

$$\frac{\partial P_j}{\partial t} + v_j \frac{\partial P_j}{\partial x} + \gamma_j P_j \frac{\partial v_j}{\partial x} = 0, \quad (3)$$

$$\frac{\partial E}{\partial x} = \sum_j q_j n_j / \epsilon_0. \quad (4)$$

Here, the electric field $E = -\partial\phi/\partial x$ and the variables n_j , P_j , and v_j are the plasma density, thermal pressure, and velocity of

species j , respectively. The subscripts $j=e$ and $j=i$ are, respectively, used for electrons and ions. m_j and q_j represent the mass and the charge of species j , respectively. For electrons $q_e = -e$ and ions $q_i = e$, ϵ_0 is the electric permittivity. In Equation (3), electrons and ions are treated as adiabatic with the same adiabatic index $\gamma_e = \gamma_i = 3$. The above set of equations is solved numerically. The spatial derivatives in these equations are solved using the fourth order central finite difference method and time derivatives are integrated using the leap-frog method to achieve second order accuracy. The details of the development of the simulation model are given in Kakad et al. (2013). We used a compensated filter to eliminate the small wavelength modes linked with such numerical noise (Lotekar et al. 2016; Kakad et al. 2016b). These numerical schemes are highly stable, and in the past, several electrostatic solitary wave

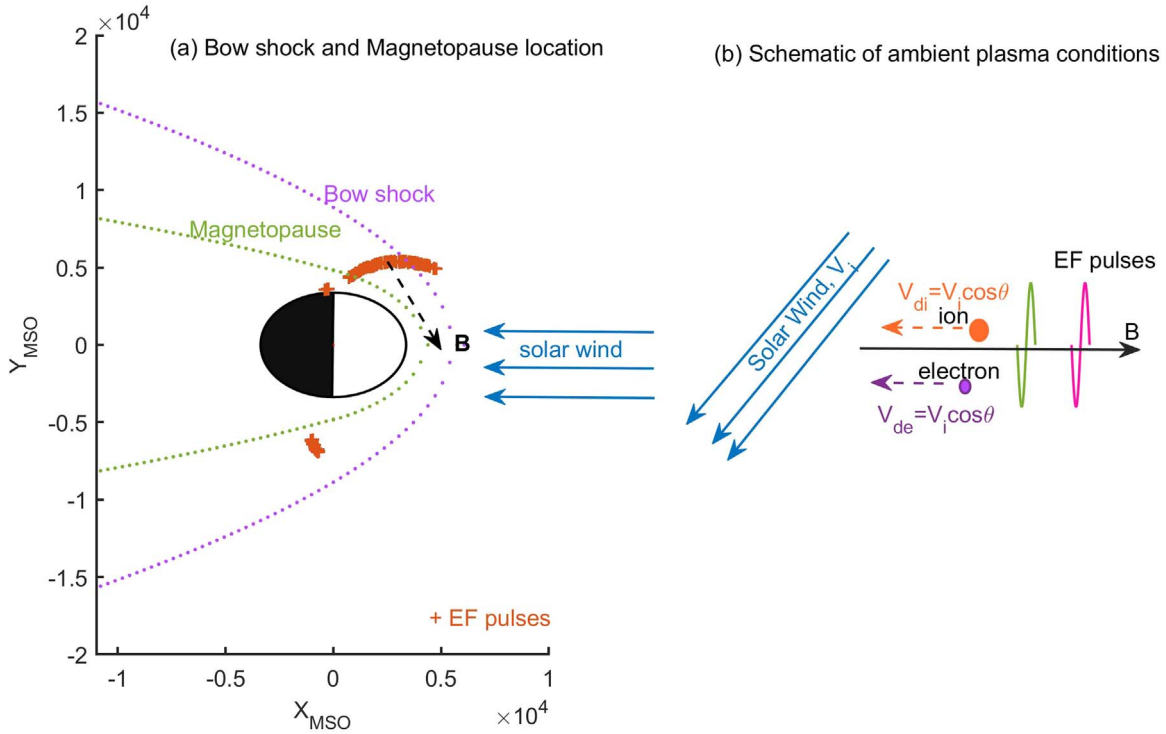


Figure 7. (a) Bow shock and magnetopause location obtained using the model proposed by Trotignon et al. (2006). The occurrence of electric field pulses is shown with the red “+” sign. The direction of the ambient magnetic field around the dusk sector is depicted by the black arrow. (b) Schematic diagram (not to scale) of the ambient plasma and magnetic field conditions along with the generated electric field pulses is illustrated.

Table 1

Electric Field Pulses Observed in Ten Time Slots during MAVEN’s Trajectory around Mars on 2015 February 9

Event	t_{start} (UT hr)	t_{end} (UT hr)	$\langle LT \rangle$ (hr)	$\langle \text{height} \rangle$ (km)
1	0.60	0.96	16.22	2604
2	2.14	2.28	5.52	3136
3	5.25	5.57	16.42	2386
4	9.78	10.26	16.49	2229
5	11.32	11.38	5.45	3042
6	14.32	14.85	16.40	2290
7	15.92	15.97	5.45	3108
8	18.92	19.43	16.41	2251
9	20.47	20.61	5.45	3179
10	23.50	23.97	16.32	2335

Note. The start time, end time, mean local time, and mean altitude during these time slots are given in their respective columns.

structures have been modeled using such fluid simulations in multispecies plasmas (Kakad et al. 2014, 2016a). Δx and Δt are respectively considered as the grid size in spatial and time domain, and their values are taken in such a way that it fulfills the Courant–Friedrichs–Lewy condition, i.e., $c \frac{\Delta t}{\Delta x} \leq 1$, which is necessary for the convergence of the explicit finite difference method. Here, c is the speed of light. We performed two simulation runs in a one-dimensional system with the periodic boundary conditions by considering the observed ambient parameters as (i) $T_e = 60$ eV, $T_i = 300$ eV, $n_{i0} = 15/\text{cc}$, $n_{e0} = 15/\text{cc}$, $V_{di} = V_{de} = -50 \text{ km s}^{-1}$ (2) $T_e = 30$ eV, $T_i = 300$ eV, $n_{i0} = 15/\text{cc}$, $n_{e0} = 15/\text{cc}$, $V_{di} = V_{de} = -50 \text{ km s}^{-1}$ (see Table 2 for more details). In the simulations, we considered the real mass ratio, i.e., $m_i/m_e = 1836$.

The background electron and ion densities satisfy the quasi-neutrality, i.e., $n_{e0} = n_{i0} = n_0$. For electron temperature, two values are considered based on the observations, i.e., 60 and 30 eV (see Figure 6(d)). The values of ω_{pi} , ω_{pe} , λ_{is} and λ_e for the considered parameters are $5.1 \times 10^3 \text{ rad s}^{-1}$, $2.18 \times 10^5 \text{ rad s}^{-1}$, 33.3 m, and 14.9 m, respectively. To initiate the simulations, we used a localized Gaussian-type initial density perturbation in the equilibrium electron and ion densities given by

$$\delta n = \Delta n \exp \left[- \left(\frac{x - x_c}{l_0} \right)^2 \right]. \quad (5)$$

Here, Δn and l_0 are the amplitude and width of the initial density perturbations, respectively. Thus, the perturbed density at $t = 0$ is $n_j(x) = n_{j0} + \delta n$. We consider the simulation system length as L_x , and $x_c = L_x/2$ is the center of the simulation system. We performed two simulation runs for the parameters given in Table 2. For these simulation runs, we consider the time interval $dt = 1 \times 10^{-3}$, the grid spacing $dx = 0.2$, system length $L_x = 7000$, $l_0 = 1$, and $\Delta n = 0.1$. Here, time is expressed in units of ω_{pi}^{-1} , space is in λ_{di} , and density is in units of n_{i0} .

The ambient plasma temperatures of ions and electrons are such that $T_i > T_e$, but $V_{thi} < V_{the}$. The ratio of $V_{the}/V_{thi} \sim 19.2$ for run-1, and $V_{the}/V_{thi} \sim 13.5$ for run-2. For such plasma conditions, we expect the presence of Langmuir and ion-acoustic modes. For simulation run-1, the space-time evolution of the electric field generated in the simulation system is shown in Figure 8(a). The $\omega - k$ dispersion obtained from the fast Fourier transform of the electric field in space and time during $t = 0 - 50\omega_{pi}$ is shown in Figure 8(b). The ion and electron plasma frequency values are marked with black horizontal dashed lines. Also, the ion-acoustic speed obtained from their linear dispersion relation

Table 2
Details of the Ambient Plasma Parameters Considered for Simulations run-1 and run-2

	n_i (/cc)	n_e (/cc)	T_i (eV)	T_e (eV)	V_{thi} (km s ⁻¹)	V_{the} (km s ⁻¹)	V_{di} (km s ⁻¹)	V_{de} (km s ⁻¹)
run-1	15	15	300	60	170	3250	-50	-50
run-2	15	15	300	30	170	2300	-50	-50

Note. n_i/n_e , T_i/T_e , V_{thi}/V_{the} , and V_{di}/V_{de} are, respectively, the ion/electron density, temperature, thermal velocity, and drift velocity.

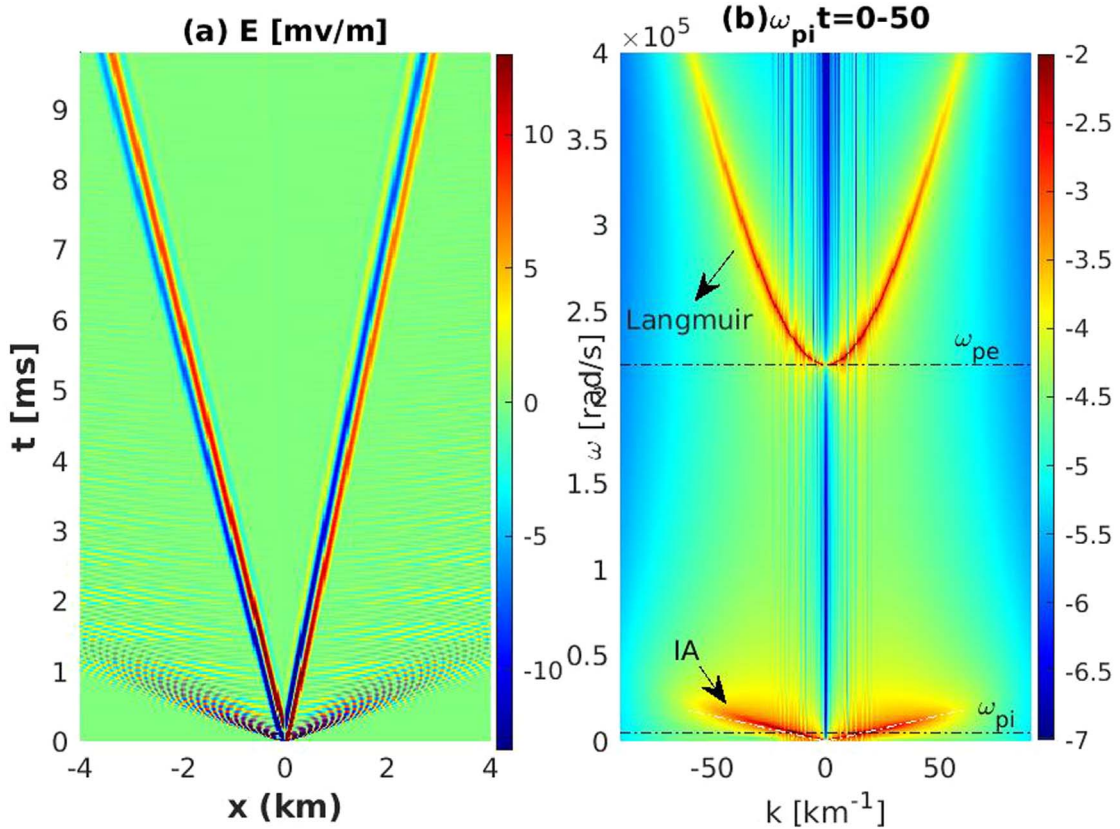


Figure 8. (a) Space-time evolution of the electric field generated in the simulation system is shown. (b) $\omega - k$ plot for the electric field generated in the simulation system is shown. The presence of Langmuir wave mode and ion-acoustic solitary waves (in the $\pm B$ direction) with speed close to $V_{IA} = 1.9V_{thi}$ are clearly visible.

$V_{IA} = \sqrt{(\gamma_e K_B T_e + \gamma_i K_B T_i)/m_i} = 1.9V_{thi}$ is shown with white dashed-dotted lines. The generation and evolution of the electric field in the simulation system are shown in a video, which is provided as supplementary material and can be directly accessed online at (<https://doi.org/10.5281/zenodo.6590897>). From Figure 8, one can see that Langmuir and ion-acoustic modes are generated in the system. The Langmuir mode is the fastest and propagates ahead of the ion-acoustic mode. We observed two nearly identical ion-acoustic solitary waves propagating parallel and antiparallel to the magnetic field, and their speeds are $V_{ph} = 1.64V_{thi}$ and $V_{ph} = -2.12V_{thi}$, respectively. To examine the characteristics of these ion-acoustic solitary waves, we tracked their maximum and minimum electric field amplitude, peak-to-peak distance (termed as width), and speed. In Figure 9, the spatial variation in electric field amplitude for the ion-acoustic solitary pulses propagating in (a) parallel to B (c) antiparallel to B , at $\omega_{pi}t = 30$ (blue color) and $\omega_{pi}t = 35$ (red color) are shown. Next, the maximum E_{max} and the absolute value of the minimum electric field $|E_{min}|$ associated with the ion-acoustic solitary pulse propagating parallel to B are plotted as a function of time in

panel (b), whereas their widths are plotted in panel (d). In Figure 9(d), the δx^R and δx^L , respectively, indicate the width of ion-acoustic solitary pulses propagating parallel and antiparallel to B . One can see that the maximum electric field amplitude evolves with time, and it approaches to nearly constant amplitude in a stable region around $\omega_{pi}t = 30-40$, which is shown by the horizontal dashed lines in panels (c) and (d). In the stable region, the speed, width, duration, maximum electric field, and maximum potential of ion-acoustic pulses propagating in parallel and antiparallel to the direction of the magnetic field are (i) $V_{ph} = 1.64 V_{thi}$, $\delta x = 5.4\lambda_{di}$, $\delta t = 0.64$ ms, $E_{max} = 8.33$ mV m⁻¹, and $\phi = 1065$ V, and (ii) $V_{ph} = 2.12V_{thi}$, $\delta x = 5.2\lambda_{di}$, $\delta t = 0.48$ ms, $E_{max} = 8.33$ mV m⁻¹, and $\phi = 1065$ mV. In a similar way, we analyzed the simulation run-2, and the speed, width, duration, maximum electric field, and maximum potential of ion-acoustic pulses propagating in parallel and antiparallel directions are (i) $V_{ph} = 1.56V_{thi}$, $\delta x = 5.6\lambda_{di}$, $\delta t = 0.70$ ms, $E_{max} = 4.13$ mV m⁻¹ and $\phi = 500$ mV, and (ii) $V_{ph} = 2.04V_{thi}$, $\delta x = 5.5\lambda_{di}$, $\delta t = 0.52$ ms, $E_{max} = 4.13$ mV m⁻¹, and $\phi = 500$ mV. In general, statistical analysis of 371 solitary waves indicates that the duration (δt) of these pulses lies in the

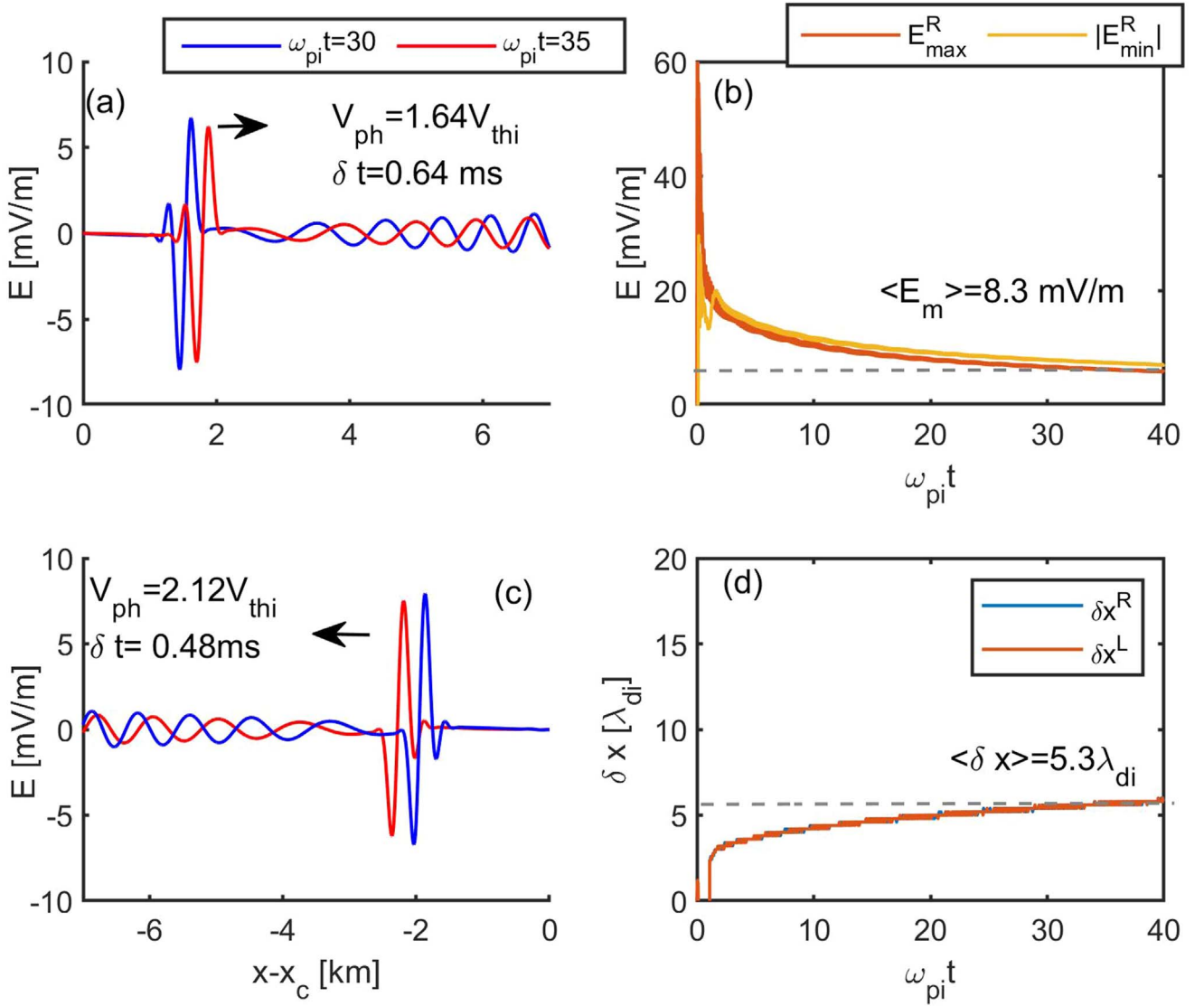


Figure 9. (a) Electric field pulse propagating in the $+B$ direction at $\omega_{pi}t = 30$ (blue color) and $\omega_{pi}t = 35$ (red color). (b) The maximum E_{\max} and the absolute value of the minimum electric field $|E_{\min}|$ associated with the electric field pulse propagating in the $+B$ direction are plotted as a function of time to track the evolution of ion-acoustic electric field pulses. The horizontal dashed line indicates the stability region, where the peak amplitude values of electric field pulses are stabilized. (c) Electric field pulse propagating in $-B$ direction at $\omega_{pi}t = 30$ (blue color) and $\omega_{pi}t = 35$ (red color). (d) The width of electric field pulses propagating parallel and antiparallel to the magnetic field is plotted as a function of time. In the stability region, the width of the electric field pulses is $5.3\lambda_{di}$.

range of 0.2–1 ms. In order to convert these durations into spatial scales, one needs information about the phase speed of these bipolar pulses. As the phase speed of these structures is not available from observations, one can use the phase speed estimated from the simulation. For run-1, the phase speed is $[1.64V_{thi}, 2.12V_{thi}]$, and for run-2, the phase speed is $[1.56V_{thi}, 2.04V_{thi}]$. Here, the two values in the square bracket represent the phase speed of ion-acoustic mode propagating parallel and antiparallel to the magnetic field. By considering these phase speeds, the 0.2–1 ms durations translate to 55–340 m, which is $\sim 1.65\text{--}10\lambda_{di}$. This exercise clearly indicates that the observed electric field pulses have spatial scales in the order of a few ion Debye-scale lengths.

In an earlier study, it was shown that the results from fluid and particle-in-cell simulations are similar for initial density perturbations of $\leq 10\%$ (Kakad et al. 2014). In our present simulations, we used an initial density perturbation of $\sim 10\%$; therefore, the results obtained from fluid and particle-in-cell

simulations are less likely to deviate. In our simulation, we used a density perturbation as a free energy source to perturb the equilibrium conditions, but one can use a velocity perturbation as well (Lotekar et al. 2019). It may be noted that most of the electric field pulses are seen in the magnetosheath region of Mars in the altitude range of 1000–3500 km. This is a region between the magnetopause boundary and bow shock boundary. In these boundary regions, the ambient plasma conditions like density and velocity change drastically and they can act as a source of perturbation for the generation of ion-acoustic waves. We cannot deny the possibility of the presence of some kinetic instability because unlike on Earth the induced mini-magnetosphere of Mars is highly dynamic. In our simulations, we could see Langmuir waves moving ahead of the ion-acoustic solitary waves. Whereas in the observations, we did not observe Langmuir-type wave packets in the vicinity of the ion-acoustic waves. As we know, the Langmuir mode is the fastest electrostatic mode,

which is generated in plasma, where $V_{\text{the}} > V_{\text{thi}}$. Its group speed is $\sqrt{3} V_{\text{the}}$ (i.e., 5630 km s^{-1}), whereas the phase speed of the ion-acoustic mode is $250\text{--}350 \text{ km s}^{-1}$ in the Martian plasma of interest in this study. This indicates that the Langmuir mode travels much faster and being a dispersive mode it will dissipate faster. In such circumstances, it is difficult to detect them in the vicinity of an ion-acoustic wave. From simulations, the estimated spatial scales of ion-acoustic waves come out to be few λ_{di} . We saw that the ion-acoustic mode drifts with a phase speed of $[2.12V_{\text{thi}}, 1.64V_{\text{thi}}]$. In the absence of ambient plasma flow, one expects the phase speed to be $1.9V_{\text{thi}}$, which is estimated from the linear dispersion relation. This change in phase speed due to the ambient plasma can give rise to a change in wave frequency of the order of $200\text{--}300 \text{ Hz}$, which is in general agreement with the frequency broadening observed in Figures 1(b) and 2(b) around the peak average spectral power.

3.4. Theoretical Analysis

In general, for the given plasma parameters, the system can support solitary wave solutions with different characteristics. The allowed range of these solutions can be obtained from nonlinear theory. For this purpose, the Sagdeev pseudo-potential technique (Sagdeev 1966) is applied, and the analytical solutions of arbitrary amplitude solitary waves in a stationary reference frame are obtained. Over the past several decades this technique has been extensively used to model plasma waves in space and astrophysical plasmas (Maharaj et al. 2013; Verheest et al. 2013; Lakhina et al. 2014). We developed a nonlinear fluid-theoretical framework by taking the ambient plasma parameters given in Table 2 and applying the Sagdeev pseudo-potential technique as detailed in Kakad et al. (2013). The Sagdeev pseudo-potential analysis provides all possible solutions of stable solitary wave structures supported by the given plasma system. The Sagdeev pseudo-potential analysis suggests that the system supports the generation of two wave modes such that one is propagating parallel and another antiparallel to the magnetic field. The Mach number of these two wave modes is represented by M^+ and M^- , respectively. We estimated the allowed range of Mach numbers of solitary waves propagating parallel and antiparallel to the magnetic field. For the parameters of run-1 and run-2, the theoretically allowed ranges of Mach numbers are $M = 1.6\text{--}2.25$ and $M = 1.52\text{--}2.14$, respectively. To demonstrate this technique, as an example, in Figures 10(a)–(c) we plotted (i) the Sagdeev pseudo-potential $S(\phi, M)$ as a function of the electrostatic potential ϕ and (ii) the associated electric field as a function of space, and the wave potential as a function of space, respectively for the Mach numbers $M^+ = 1.62$ and 1.63 by considering the parameters of run-1. As the Mach numbers of these solitary pulses are available, one can deduce the duration of the solitary pulses. The allowed range of Mach numbers, electric field amplitudes, maximum potential, widths, and time durations of ion-acoustic solitary wave pulses are given in Table 3 for the plasma parameters of run-1 and run-2. From Table 3, one can see that the maximum electric field and time durations allowed by theory for the plasma parameters of run-1 and run-2 are in excellent agreement with nonlinear theory. In Figure 10(d), we plotted E_{max} as a function of δt observed by MAVEN in the magnetosheath region of Mars. We included the E_{max} and δt of the modeled ion-acoustic solitary wave

pulses obtained through simulations (red: run-1, and blue: run-2) and theory (green). One can see that the characteristics of the modeled solitary pulses are in good agreement with the observations. This confirms that most of the ion Debye-scale electric field pulses observed in the magnetosheath region of Mars are ion-acoustic solitary waves.

4. Summary and Conclusions

In this paper, we have presented a comprehensive analysis of 450 solitary pulses observed by the MAVEN spacecraft during its five passes around Mars on 2015 February 9. We focused on the 371 bipolar pulses that were observed at an altitude of $1000\text{--}3500 \text{ km}$ in the Martian magnetosheath. We modeled these pulses with both nonlinear fluid theory and simulations. We compared the electric field amplitudes and durations of the observed pulses with the modeled ion-acoustic solitary wave structures. We found that the electric field amplitudes and durations of the observed pulses by MAVEN are in good agreement with both theory and simulations. Thus, the observed bipolar pulses are identified as ion-acoustic solitary wave structures with a speed close to the ion-acoustic speed. The theory and simulation suggest that the bipolar pulses are associated with the positive wave potentials. The salient features of these solitary pulses are given below.

1. The observed bipolar electric field pulses propagate in the direction quasi-parallel to the ambient magnetic field and thus they are identified as electrostatic structures.
2. The electric field strength of these pulses varies between 1 and 25 mV m^{-1} .
3. The bipolar pulses are dominantly seen in the dawn, $5\text{--}6 \text{ LT}$, and dusk sector $15\text{--}18 \text{ LT}$ at altitudes of $1000\text{--}3500 \text{ km}$.
4. The duration and frequency of electric field pulses are predominantly seen in the range of $0.2\text{--}1 \text{ ms}$ and $1\text{--}5 \text{ kHz}$, respectively. In terms of spatial scale, it comes out to be $\sim 1.65\text{--}10 \lambda_{\text{di}}$.
5. It is found that the observed bipolar pulses have frequencies close to the ion plasma frequency, such that $f_{\text{pi}} \leq f_{\text{ef}} \ll f_{\text{pe}}$. This confirms that the pulses are ion-acoustic type solitary waves.

When the solar wind interacts with the atmosphere of Mars, there the a possibility of the presence of reflected ions from Mars' bow shock. The presence of such a reflected plasma population close to the bow shock region has been reported earlier (Scholer et al. 1993; Eastwood et al. 2005). In such a scenario, there is the possibility of the generation of ion holes through the nonlinear growth of ion streaming instability. Thus, ion streaming instability can be another possible mechanism to explain the generation of the observed bipolar electric field in the magnetosheath region of Mars. When this instability grows and saturates, it can form ion holes. The growth rate of the ion streaming instability is dependent on the density, speed, and temperature of the reflected ions (Akimoto & Winske 1985). In earlier theoretical studies, it has been shown that the generation of ion holes is limited to the plasmas having $T_i/T_e < 0.3$ (Schamel 1982). However, a recently developed theoretical model supports the generation of ion holes for $T_i/T_e > 0.3$ as well (Aravindakshan et al. 2020). The generation of ion holes in such plasmas is reported by Wang et al. (2020), where $T_i/$

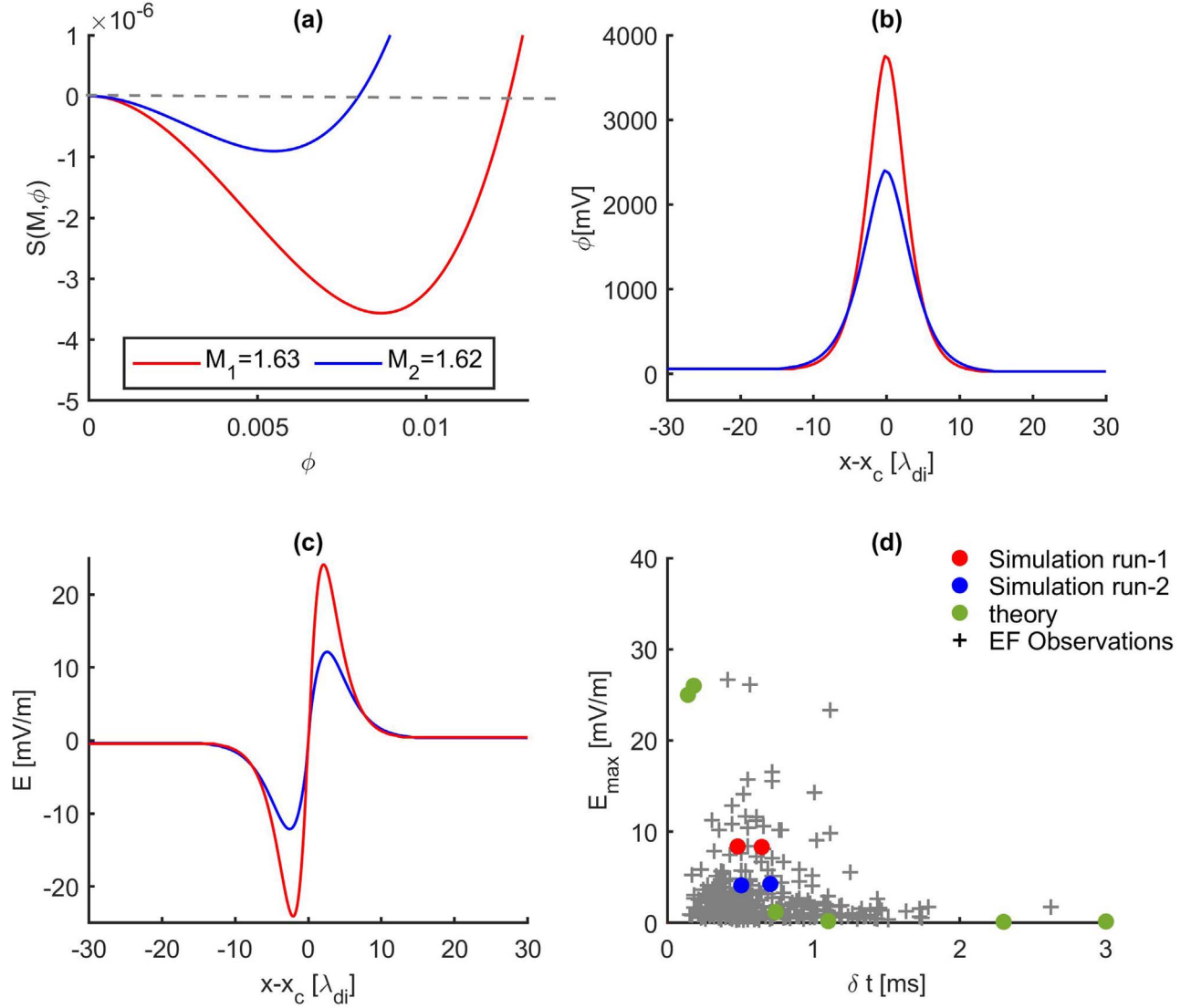


Figure 10. For the plasma parameters of run-1, as an example, the variation in (a) the Sagdeev pseudo-potential $S(\phi, M)$ as a function of electrostatic potential ϕ and their (b) electric field and (c) potential as a function of space are plotted for Mach numbers $M^\pm = 1.62$ and 1.63 . In panel (d), E_{max} is plotted as a function of δt for the electric field observed by MAVEN in the magnetosheath region of Mars, and are superimposed with the modeled E_{max} and δt of ion-acoustic solitary wave pulses obtained from (i) simulations (red: run-1 and blue: run-2) and (ii) theory (green).

Table 3

Allowed Range of Characteristics (Mach Number, Maximum Potential, Electric Field, Width, and Duration) of Ion-acoustic Solitary Waves Generated in a System Supported by the Ambient Plasma Parameters Given in Table 2

	Mach No (V_{thi})	ϕ_{max} (mV)	E_{max} ($mV m^{-1}$)	Width (δx) (λ_{di})	δt (ms)
run-1	$M^+ = 1.6-1.66$	135–7100	0.16–69	24–2	3–0.25
	$M^- = 2.19-2.25$	118–7300	0.12–72	26–2	2.3–0.18
run-2	$M^+ = 1.52-1.55$	268-1903	1.2-26	5.9–1.4	0.74–0.18
	$M^- = 2.11-2.14$	80–1854	0.2–25	11-1.53	1.1–0.14

Note. These allowed ranges of parameters were obtained using the Sagdeev pseudo-potential technique. The superscripts “+” and “–” in the Mach number range represent the ion-acoustic solitary pulse moving parallel and antiparallel to the ambient magnetic field.

$Te \sim 0.4$. In Mars’ magnetosheath, there are electron and ion temperatures such that $T_i/T_e \sim 5$; thus, there is the possibility of the generation of ion holes in the present plasma model. However, these ion holes are associated with negative electrostatic potential. The question is, can we confirm the polarity of the electrostatic potential from MAVEN observations? It may be noted that we do not have information on the

drift and calibrated potential associated with these bipolar pulses as it is single spacecraft observations, and the LPW instrument records the electric field in one direction only. With the multi-spacecraft measurements or three-dimensional electric field measurements (Steinvall et al. 2021) or information on boom potential with respect to the spacecraft potential (Vasko et al. 2020), it is possible to estimate the drift speed and


potential associated with these structures by using interferometry. To conclude, we have demonstrated that the observed bipolar electric field pulses by MAVEN are ion-acoustic solitary wave structures as they are in good agreement with the observations. At the same time, one cannot rule out the possibility of the presence of ion holes as the reflected ions from Mars' bow shock can generate ion holes through ion streaming instability. A detailed investigation of this possibility is left for future work.

All calibrated data used in the present study is available on the Planetary Data System at (<https://pds-ppi.igpp.ucla.edu/>). The authors are thankful to L. Andersson for the LPW/MAVEN data and the assistance provided to understand the electric field data. Authors thank J.E.P. Connerney for providing access to MAG/MAVEN data, D.L. Mitchell for SWEA/MAVEN data, J.S. Halekas for SWIA/MAVEN data, and P.A. Dunn for key parameters. I.K. and A.K. gratefully acknowledge financial support from project FSU-2021-012/8474000352, funded by Khalifa University of Science and Technology, Abu Dhabi, UAE. Authors I.K. and H.A. also gratefully acknowledge support from the Abu Dhabi Department of Education and Knowledge (ADEK), currently ASPIRE UAE, via an Abu Dhabi Award for Research Excellence (AARE-2018, grant ADEK/HE/157/18). The hospitality offered by Khalifa University to A.K. and to H.A. during their research visit in 2021 and in 2022 is greatly appreciated. I.K. gratefully acknowledges financial support from Khalifa University's Space and Planetary Science Center under grant No. KU-SPSC-8474000336. The model computations were performed on the High Performance Computing System at the Indian Institute of Geomagnetism.

ORCID iDs

Bharati Kakad  <https://orcid.org/0000-0001-8440-3373>

Amar Kakad  <https://orcid.org/0000-0002-1308-4245>

Harikrishnan Aravindakshan  <https://orcid.org/0000-0003-4663-4255>

Ioannis Kourakis  <https://orcid.org/0000-0002-4027-0166>

References

Akbari, H., Andersson, L., Peterson, W., et al. 2019, *JGRA*, **124**, 4518

- Akimoto, K., & Winske, D. 1985, *JGRA*, **90**, 12095
- Andersson, L., Ergun, R., Delory, G., et al. 2015, *SSRv*, **195**, 173
- Aravindakshan, H., Yoon, P. H., Kakad, A., & Kakad, B. 2020, *MNRAS: Lett.*, **497**, L69
- Bale, S., Kellogg, P., Larsen, D., et al. 1998, *GeoRL*, **25**, 2929
- Connerney, J., Espley, J., Lawton, P., et al. 2015, *SSRv*, **195**, 257
- Eastwood, J., Lucek, E., Mazelle, C., et al. 2005, *SSRv*, **118**, 41
- Ergun, R., Carlson, C., McFadden, J., et al. 1998, *PhRvL*, **81**, 826
- Grard, R., Pedersen, A., Klimov, S., et al. 1989, *Natur*, **341**, 607
- Halekas, J., Taylor, E., Dalton, G., et al. 2015, *SSRv*, **195**, 125
- Harada, Y., Andersson, L., Fowler, C., et al. 2016, *JGRA*, **121**, 9717
- Kakad, A., Kakad, B., Anekallu, C., et al. 2016a, *JGRA*, **121**, 4452
- Kakad, A., Kakad, B., Lotekar, A., & Lakhina, G. 2019, *PhPI*, **26**, 042112
- Kakad, A., Lotekar, A., & Kakad, B. 2016b, *PhPI*, **23**, 110702
- Kakad, A., Omura, Y., & Kakad, B. 2013, *PhPI*, **20**, 062103
- Kakad, B., Kakad, A., & Omura, Y. 2014, *JGRA*, **119**, 5589
- Lakhina, G., Singh, S., & Kakad, A. 2014, *PhPI*, **21**, 062311
- Lakhina, G., Singh, S., Kakad, A., & Pickett, J. 2011, *JGRA*, **116**, A10218
- Lotekar, A., Kakad, A., & Kakad, B. 2016, *PhPI*, **23**, 102108
- Lotekar, A., Kakad, A., & Kakad, B. 2019, *PhPI*, **26**, 100701
- Lundin, R., Winningham, D., Barabash, S., et al. 2006, *Sci*, **311**, 980
- Ma, Y., Nagy, A. F., Sokolov, I. V., & Hansen, K. C. 2004, *JGRA*, **109**, A07211
- Maharaj, S., Bharuthram, R., Singh, S., & Lakhina, G. 2013, *PhPI*, **20**, 083705
- Malaspina, D. M., Goodrich, K., Livi, R., et al. 2020, *GeoRL*, **47**, e2020GL090115
- Matsumoto, H., Kojima, H., Miyatake, T., et al. 1994, *GeoRL*, **21**, 2915
- Mitchell, D., Mazelle, C., Sauvaud, J.-A., et al. 2016, *SSRv*, **200**, 495
- Mozer, F., Bonnell, J., Hanson, E., Gasque, L., & Vasko, I. 2021a, *ApJ*, **911**, 89
- Mozer, F. S., Vasko, I. Y., & Verniero, J. 2021b, *ApJL*, **919**, L2
- Nagy, A., Winterhalter, D., Sauer, K., et al. 2004, *SSRv*, **111**, 33
- Omura, Y., Matsumoto, H., Miyake, T., & Kojima, H. 1996, *JGRA*, **101**, 2685
- Pérez-de Tejada, H. 1987, *JGRA*, **92**, 4713
- Pickett, J. 2021, *JGRA*, **126**, eJA029548
- Romanelli, N., Modolo, R., Leblanc, F., et al. 2018, *GeoRL*, **45**, 7891
- Sagdeev, R. 1966, *RvPP*, **4**, 23
- Schamel, H. 1982, *PhyS*, **1982**, 228
- Scholer, M., Fujimoto, M., & Kucharek, H. 1993, *JGRA*, **98**, 18971
- Steinvall, K., Khotyaintsev, Y. V., & Graham, D. B. 2022, *JGRA*, **127**, e30143
- Tao, J., Ergun, R., Newman, D., et al. 2012, *JGRA*, **117**, A03106
- Trotignon, J., Mazelle, C., Bertucci, C., & Acuña, M. 2006, *P&SS*, **54**, 357
- Trotignon, J. G., Grard, R., & Savin, S. 1991, *JGRA*, **96**, 11253
- Vaisberg, O., Ermakov, V., Shuvalov, S., et al. 2017, *P&SS*, **147**, 28
- Vaisberg, O., Ermakov, V., Shuvalov, S., et al. 2018, *JGRA*, **123**, 2679
- Vasko, I. Y., Wang, R., Mozer, F. S., Bale, S. D., & Artemyev, A. V. 2020, *FrP*, **8**, 156
- Verheest, F., Hellberg, M. A., & Kourakis, I. 2013, *PhPI*, **20**, 082309
- Wang, R., Vasko, I., Mozer, F., et al. 2020, *ApJL*, **889**, L9
- Williams, J., Chen, L.-J., Kurth, W., Gurnett, D., & Dougherty, M. 2006, *GeoRL*, **33**, L06103